J. Fluid Mech. (2009), *vol.* 634, *pp.* 463–486.
doi:10.1017/S0022112009007605 Printed in the United Kingdom

Migration and deformation of bubbles rising in a wall-bounded shear flow at finite Reynolds number

FUMIO TAKEMURA[1], JACQUES MAGNAUDET[2]†
AND PANAGIOTIS DIMITRAKOPOULOS[3]

[1]National Institute of Advanced Industrial Science and Technology 1-2-1 Namiki,
Tsukuba, Ibaraki 305-8564, Japan

[2]Institut de Mécanique des Fluides de Toulouse, UMR CNRS/INPT/UPS 5502,
Allée Camille Soula, 31400 Toulouse, France

[3]Department of Chemical and Biomolecular Engineering, University of Maryland,
College Park, MD 20742, USA

(Received 26 March 2008 and in revised form 6 April 2009)

The quasi-steady migration and deformation of bubbles rising in a wall-bounded linear shear flow are investigated experimentally in the low-but-finite-Reynolds-number regime. A travelling optical device that follows the bubble is used for this purpose. This apparatus allows us to determine accurately the bubble radius, contour and rising speed, together with the distance between the bubble and the wall. Thereby the transverse component of the hydrodynamic force is obtained for Reynolds numbers Re (based on the bubble diameter and slip velocity of the bubble in the undisturbed shear flow) less than 5. The results indicate that in the range $0.5 < Re < 1.5$, the transverse force acting on a spherical bubble agrees well with an extension of the theoretical solution obtained by McLaughlin (*J. Fluid Mech.*, vol. 246, 1993, pp. 249–265) for rigid spheres, whereas it becomes larger than the theoretical prediction for $Re > 1.5$. In the regime in which bubble deformation is significant, the shape of the bubble and the deformation-induced transverse force are determined both experimentally and computationally, using a spectral boundary element method. Both estimates are found to be in good agreement with each other, while the theory of Magnaudet, Takagi & Legendre (*J. Fluid Mech.*, vol. 476, 2003, pp. 115–157) is found to predict accurately the deformation but fails to predict quantitatively the deformation-induced transverse force.

1. Introduction

Predicting how buoyant particles and bubbles migrate horizontally in a vertical pipe flow is of central importance in estimating the averaged characteristics of the corresponding widespread two-phase flow, including the local volume fraction of the dispersed phase, wall friction and heat exchange through the wall (see e.g. Serizawa, Kataoka & Michiyoshi 1975 for the case of gas bubbles). Nevertheless, this prediction is made difficult by the fact that any particle moving in a wall-bounded shear flow experiences two different types of inertial transverse (or lift) forces which generally

---

† Email address for correspondence: jacques.magnaudet@imft.fr

combine nonlinearly, one of which is due to the local shear, while the other results directly from the presence of the wall. Things are even more complex with bubbles and drops which may deform in such a flow and undergo an additional deformation-induced transverse force. Inertial migration of rigid particles in wall-bounded shear flows has attracted attention since the pioneering experiments of Segré & Silberberg (1962*a*, *b*) involving neutrally buoyant spheres. We refer the reader to the papers by Leal (1980), McLaughlin (1991) and Hogg (1994) for the case of such particles and to that by Magnaudet, Takagi & Legendre (2003; hereinafter referred to as MTL) for the case of buoyant drops and bubbles experiencing a near-wall migration due to the combined effect of inertia and deformation. Here we only briefly discuss the available literature concerned with the lateral migration of particles moving near a wall in a linear shear flow in the low-but-finite-Reynolds-number regime, with a special emphasis on the case of bubbles.

When a buoyant sphere migrates in an unbounded linear shear flow, both the slip velocity U_s and the shear-induced velocity GR (where G denotes the shear rate and R is the sphere radius) contribute to the nonlinearity of the governing equations and hence to the generation of the transverse force. This is why this force depends in general on the ratio between the Stokes length ν/U_s and the Saffman length $(\nu/|G|)^{1/2}$, with ν denoting the kinematic viscosity. When the flow is bounded by a rigid flat wall, the disturbance depends in addition on the separation distance L between the particle and the wall, and so does the lift force.

If the separation is much less than the Stokes and Saffman lengths, the wall lies within the inner region of the disturbance, and the leading contribution to the wall-induced lift force may be obtained through a regular expansion technique with respect to the particle Reynolds number (Cox & Brenner 1968). Cox & Hsu (1977) took advantage of this to obtain the lateral force on a rigid sphere moving parallel to the wall in a linear shear flow bounded by a single wall, assuming $L/R \gg 1$. Cherukat & McLaughlin (1994) evaluated numerically the volume integral required to obtain the lift force by means of the reciprocal theorem and expanded the result with respect to L/R to obtain higher-order contributions with respect to R/L which are useful when the particle is close to the wall. The case of a drop of arbitrary viscosity moving either along a wall or perpendicular to it was considered by MTL using similar techniques. In contrast, the case in which the wall lies in the outer region of the disturbance, i.e. $LU_s/\nu \gg 1$ and $L(|G|/\nu)^{1/2} \gg 1$, requires the use of matched asymptotic expansions. After several attempts, this situation was worked out by McLaughlin (1993) who succeeded in obtaining the lift force on a rigid sphere moving parallel to a wall in a linear shear flow in an integral form.

In addition to the above inertial effects, bubbles and drops migrating in a wall-bounded shear flow experience deformation because of the shear present in the undisturbed flow as well as because of the extra shear resulting from the structure of the near-wall disturbance. If the capillary numbers $\mu U_s/\sigma$ and $\mu GR/\sigma$ are both small (μ being the dynamic viscosity of the suspending fluid and σ the interfacial tension), the total deformation may be obtained by summing the effects of the above two shears. Takemura *et al.* (2002; hereinafter referred to as TTMM) determined experimentally the deformation experienced by a bubble rising near a vertical wall in a quiescent liquid and found their results to agree well with the theoretical prediction of MTL. This deformation in turn results in a transverse force which, for a buoyant drop or bubble, was evaluated by the same authors. Both the theory and the experiments indicate that the magnitude of the deformation-induced lift force is comparable to that of the inertial lift force when the Reynolds number is comparable to the capillary number, the total lift force then being the sum of the two elementary contributions.

As pointed out in TTMM, very few experiments to date provide reliable data for the variations of the lateral force on a particle moving in the vicinity of a wall as a function of the various parameters of the problem, and even fewer have considered drops or bubbles. In particular we are not aware of any available experiment in which the transverse force acting on a drop or a bubble moving close to a wall in a simple shear has been determined. The goal of the present study is to obtain such data in order to check existing theories for the lateral force, clarify their limitations and propose reasonable extensions if necessary. To this end, we produce a quasi-linear shear flow by moving two parallel belts in opposite directions and measure optically the migration velocity of bubbles rising near one of the belts (§ 2). Then we estimate the quasi-steady lift force on spherical bubbles in the regime $0.5 < Re < 5$ (where $Re = 2RU_s/\nu$) and compare them with a generalized form of the analytical prediction of McLaughlin (1993) (§ 3). In § 4, we address situations in which the effect of bubble deformation is significant. We estimate separately the effect of the undisturbed shear and that of the shear induced by the near-wall disturbance on the deformation for $0.1 < Re < 0.5$ and compare the corresponding results with two independent predictions. The first of these is provided by the theory of MTL, which is based on the domain perturbation method and treats the influence of the nearby wall through a reflection technique. The other one, which is part of the present work, results from a numerical determination of the evolution of a deformable bubble in a wall-bounded linear shear flow. The corresponding results are obtained by using the fully implicit interfacial spectral boundary element method developed by Dimitrakopoulos (2007). Owing to the intrinsic limitations of the boundary element formulation, these computations are performed under creeping flow conditions. However, for reasons explained below, they are suitable for obtaining the leading-order bubble deformation and deformation-induced transverse force in the weakly inertial regime considered in § 4.

To our knowledge, the present study provides the first detailed measurements of the inertial transverse force acting on a clean spherical bubble rising parallel to a wall in a linear shear flow. In cases in which the bubble deforms significantly and takes a spheroidal shape, it also provides original experimental and computational results regarding the interface deformation and the corresponding associated lateral force. In both cases, both positive and negative shears are considered, corresponding to situations in which wall effects and shear effects act either in a cooperative way or in an antagonistic manner.

2. Experimental apparatus and procedure

Figure 1 shows a diagram of the experimental facility used to measure the evolution of the bubble radius R, rising speed U_b, horizontal bubble velocity W (positive towards the fluid interior) and distance between the bubble centre and the wall L. The facility consists of a test section and an optical measurement system. The test section is a 600 mm long acrylic channel with a cross-section of 280 × 130 mm. We use two stainless steel belts to produce a quasi-linear shear flow by moving two parallel belts in opposite directions. The width and thickness of the belts are 40 mm and 0.1 mm, respectively. The distance H between the two belts is 50 mm, and the length of the parallel section between the belts is 400 mm. The stainless steel belts were manufactured by joining both edges of a plate with an initial thickness of 0.3 mm.

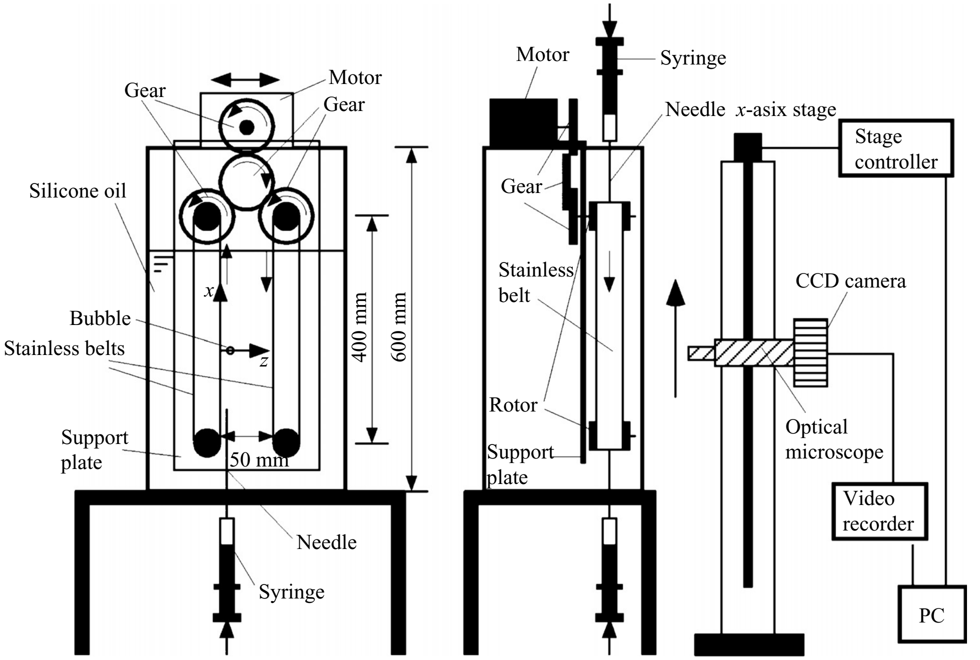

(*a*) Front view of the test section (*b*) Side view of the test section and the optical measurement system

FIGURE 1. Sketch of the experimental device.

Since the roughness at the joint may produce disturbances in the flow, the belts were thinned down to 0.1 mm by a rolling mill process. The two belts are tightened by four rotors fixed on the support plate. Two gears connected to the upper two rotors are rotated by a single motor, which allows the two belts to rotate with exactly the same speed. Although the rotation speed of the motor can be arbitrarily set from 0 to 100 rpm, we limit it to 25 rpm to reduce the vibration of the belts below 10 µm. In this range, the wall speed U_w can be varied from -52 to 52 mm s^{-1}, so that the maximum shear rate is 2.08 s^{-1}. Single bubbles are produced through a needle connected to the tip of a syringe, either from the bottom of the tank or from its top when the shear is positive, since the bubble is going down in the latter case. The two needles are inserted in the bottom (respectively top) part of the test section, and their tips are fixed approximately 30 mm above (respectively below) the centre of the bottom (respectively top) rotor. The syringe is slowly pressurized by a syringe pump (MD-1001, Bioanalytical System Inc.) to introduce bubbles into the test section. The support plate can be moved horizontally on a rail fixed on the test section and the distance between the needle and the belts can be adjusted arbitrarily. In the following, we define the vertical and horizontal directions as the x- and z-axis, respectively.

The velocity distribution U_f in the flow produced by the moving belts was determined by means of a laser-Doppler anemometry system (Smart LDV Model 8739, Kanomax). We measured the horizontal distribution of the vertical and horizontal velocities every 50 mm between $x=0$ mm and $x=300$ mm above the tip of the needle at $z=1$, 2, 3, 4, 5, 7 and 10 mm from the wall; 5000 velocity data were obtained at each measurement point. Figure 2 shows the vertical velocity profiles at $x=0$, 50, 100, 250 and 300 mm when the flow Reynolds number defined as $Re_f=HU_w/\nu$ is 123 (corresponding to $U_w=51.5$ mm s^{-1} and $\nu=20.9$ mm^{-2} s^{-1}). Figure 2 reveals

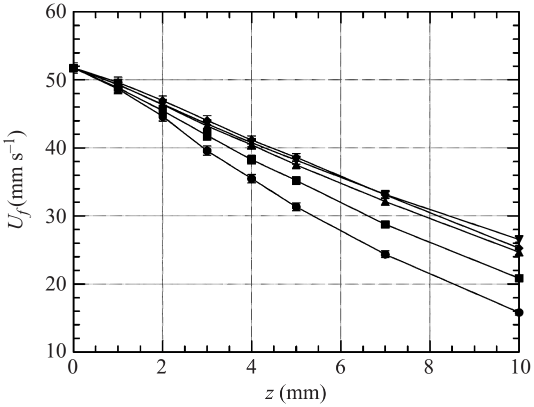

FIGURE 2. Vertical velocity distribution in the quasi-linear shear flow at various vertical positions: ●, 0 mm; ■, 50 mm; ▲, 100 mm; ◆, 250 mm; ▼, 300 mm.

that the velocity profile does not significantly evolve in the streamwise direction for $x \geqslant 100$ mm, so that the flow may be considered fully developed downstream of the entrance region. Moreover this figure reveals that in the same range of x, the curvature of the velocity profile in the z-direction is very small, so that the flow may be considered linear for $x \geqslant 100$ mm. Expressing the velocity distribution in the form $U_f(z) = U_w + Gz$, we estimated G by correlating the measured velocity data. The results indicate that in the near-wall region $z \leqslant 10$ mm concerned with our measurements, the local velocity gradient differs from the averaged shear rate G by less than 10 % for 50 mm $< x < 100$ mm and by less than 3 % for $x \geqslant 100$ mm. Therefore the experimental data to be discussed below were all taken in this fully developed region $x \geqslant 100$ mm. We finally calculated the local slip velocity of a bubble standing at the current lateral position z as $U_s(z) = U_b - U_f(z)$.

The optical part of the measuring system was developed by Takemura & Yabe (1998, 1999) and has already been described by TTMM. In brief, this device combines a charged-couple device (CCD) camera with a microscope in order to measure accurately the radius of the bubble (see figure 1*b*). The CCD camera has 640 × 480 pixels which, according to the calibration used in the present study, yield a resolution of about 6.4 μm pixel^{-1}. The depth of field of the microscope is about 150 μm. The reader may refer to the papers by TTMM and Takemura & Magnaudet (2003) for details on how the verticality of the wall is adjusted and how the separation distance between the bubble and the wall is precisely determined. In the present experiments, we adjust the horizontal distance between the two belts within ± 30 μm. To track the rising bubble, we adjust the speed of the camera as follows. A picture of the bubble is recorded on the computer via the video capture board at a rate of 30 frames s^{-1}. A binary image is made, and the position of the bubble is determined. Then we calculate the relative velocity between the bubble and the camera from consecutive frames and use this relative velocity to adjust the speed of the vertical displacement system.

Using the device and the adjustments described above, the bubble radius, rising speed and separation distance between the bubble and the wall are measured from the recorded pictures and the time history of the camera speed. The radius R and separation distance L are evaluated on each frame, while the local speed of the bubble is obtained by locating the centre of the bubble, calculating the relative speed from the movement of the centre in two consecutive frames and adding the speed of the

	K20	K50	K100	K200
ρ (kg m^{-3})	948	955	965	968
μ ($\times 10^3$; kg m^{-1}s^{-1})	19.6	44.6	100.4	176.2
ν ($\times 10^6$; m^2 s^{-1})	20.6	46.7	104.0	182.1
σ ($\times 10^3$; kg s^{-2})	20.8	20.8	20.9	21.1

TABLE 1. Physical properties of the silicone oils at temperature $T = 20°$C.

camera corresponding to these two frames. The migration velocity W of the bubble in the z-direction is calculated from the distance L obtained every 1/30 s. Assuming that W can be expressed as a power law of L, i.e. $W = \mathrm{d}L/\mathrm{d}t = AL^B$, the trajectory of the bubble is determined as a function of time by integrating this power law. After the discrete values of L have been fitted, the coefficients A and B are determined through a least square procedure. The uncertainties affecting the various quantities can be quantified as follows. The uncertainty on R is 1 pixel, i.e. about 6.4 μm, whereas that on L is twice as large because the wall is somewhat out of focus. The uncertainty on the relative speed between the bubble and the camera is about 0.4 mm s^{-1}; i.e. the relative error on U_b is about 2 % when the bubble rises with a speed of 20 mm s^{-1}. Using these estimates, we evaluated the uncertainties on quantities such as U_s and L/R by using standard techniques (Benedict, Abernethy & Osolsobe 1985).

Determining precisely L in cases in which the bubble is not perfectly spherical requires the position of the bubble centroid to be properly defined. For this purpose, we choose an initial approximation of the centroid location (defined as $r = 0$), express the bubble contour as $r = g(\theta)$ and perform a Fourier decomposition of this contour (see figure 8). In such a decomposition, terms in $\cos\theta$ and $\sin\theta$ are associated with a translational mode and become zero if the origin $r = 0$ coincides with the geometrical centroid. We apply this condition iteratively to reduce the strength of the translational mode and obtain the position of the centroid at convergence.

All the experiments are carried out at room temperature and atmospheric pressure using silicone oil (dimethyl siloxane polymer; KF-96, Shinetsu Chemical Co.) as the carrying liquid. To cover the range $Re < 5$ ($Re = 2RU_s/\nu$), we employ four different qualities of silicone oil with kinematic viscosities ranging from about 2.0×10^{-5} m^2 s^{-1} to 2.0×10^{-4} m^2 s^{-1}. The physical properties of these oils are detailed in table 1; hereinafter these various oils are referred to as K20 to K200, according to the denomination specified in table 1. Variations of oil viscosity with temperature are determined using a rotating Couette viscometer, and the corresponding corrections are taken into account in the data analysis. Moreover the temperature of the device is determined before and after each set of experiments in order to ensure that no significant temperature variation has occurred in between. An important property of silicone oil is its non-polar nature. Because of this, no indication of surface contamination was detected during the analysis of the experimental results. In particular the values of the drag force acting on bubbles rising far from the wall were always found to agree well with values corresponding to clean bubbles subject to a shear-free boundary condition (see Takemura & Magnaudet 2003 for details).

Figure 3 shows typical CCD camera photographs of a single spherical bubble with $R = 0.59$ mm rising near the wall in presence of three different wall velocities. The

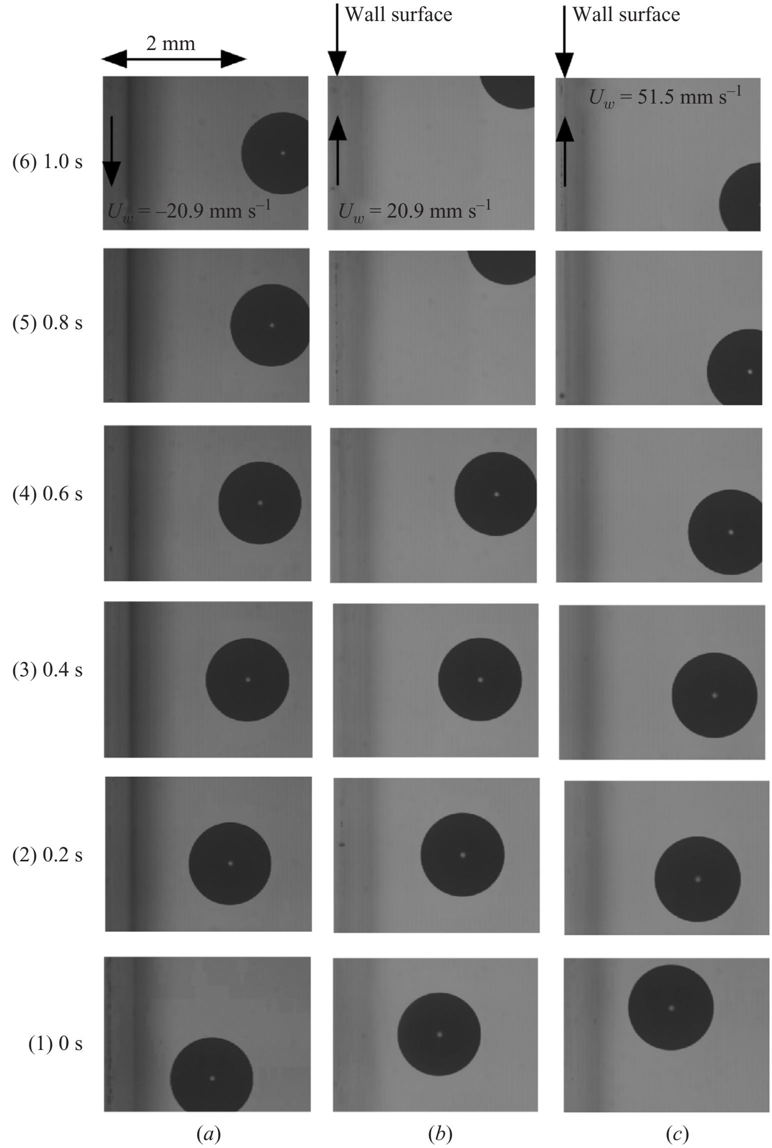

FIGURE 3. Photographs showing three typical bubble trajectories in a wall-bounded linear shear flow (K20, $R = 0.59$ mm, $U_{s\infty} = 47.4$ mm s^{-1}, $Re_\infty = 2.7$). The only change between the three series lies in the wall velocity: (*a*) $U_w = -20.9$ mm s^{-1}; (*b*) $U_w = 20.9$ mm s^{-1}; (*c*) $U_w = 51.5$ mm s^{-1}.

carrying liquid is the K20 silicone oil, and the bubble slip velocity $U_{s\infty}$ far from the wall is 47.4 mm s^{-1}, corresponding to a slip Reynolds number $Re_\infty = 2.7$. In all three cases, the bubble centre lies initially at 1.38 mm from the wall. Comparing the horizontal position of the bubble at a given time for all three series clearly indicates that the migration velocity W increases from left to right. Since the shear rate decreases from case (*a*) to case (*c*) (going from positive to negative values), figure 3 leads us to the conclusion that the migration velocity increases as the shear rate G decreases. This is qualitative agreement with the theoretical prediction of the migration velocity W

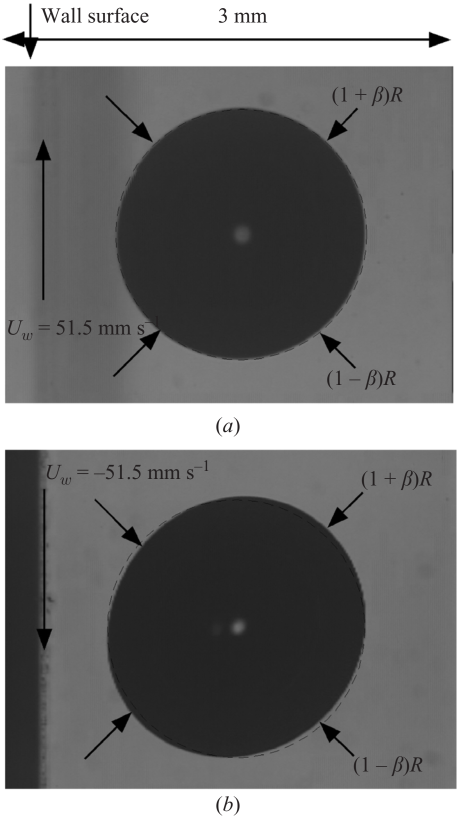

FIGURE 4. Two examples of a slightly deformed bubble rising in a wall-bounded linear shear flow (K100, $R = 0.85$ mm, $L \approx 1.3$ mm $U_{s\infty} = 21.8$ mm s^{-1}, $Re_\infty = 0.36$): (*a*) $U_w = 51.5$ mm s^{-1}; (*b*) $U_w = -51.5$ mm s^{-1}.

obtained by MTL who showed that provided $LU_s/\nu \ll 1, LGR/\nu \ll 1$ and $L/R \gg 1$, one has at leading order in terms of R/L

$$W = \frac{1}{16}U_s\left(\frac{RU_s}{\nu} - \frac{11}{6}\frac{RGL}{\nu}\right). \tag{1}$$

We note for future purpose that (1) indicates that within its regime of validity, W can be expressed as the sum of the near-wall migration velocity in a quiescent fluid and the shear-induced migration velocity.

When the ratio between viscous and capillary forces (i.e. the capillary number) increases, the effect of bubble deformation becomes significant. TTMM showed that in a quiescent liquid, the shear created around the bubble by the no-slip condition at the wall is responsible for this deformation and that the bubble is lengthened (respectively shortened) along an axis inclined at 45° (respectively –45°) from horizontal. When the bubble rises in a wall-bounded shear flow, the above deformation combines with that induced by the undisturbed shear. Figure 4 shows two typical photographs taken in this situation for the same value of L but with two different values of U_w, the wall velocity in case (*a*) (respectively *b*) corresponding to a negative (respectively positive) shear rate. The photographs indicate that although the distance L is the same, the deformation in case (*b*) is larger than that in case (*a*). Assuming that the bubble

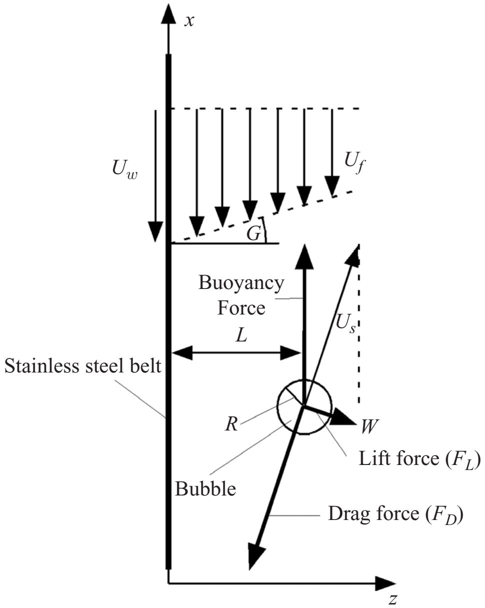

FIGURE 5. The force balance on the bubble in a situation corresponding to $U_w < 0$ and $G > 0$.

deforms in the (x, z) plane as an ellipsoid without any volume change, we quantify its deformation β through the ratio ζ between the length of its major axis and that of its minor axis, i.e. $\zeta = (1+\beta)/(1-\beta)$. Using this definition, we find $\beta \approx 0.01$ in case (a) and $\beta \approx 0.04$ in case (b), which indicates that the deformation increases with the shear rate G.

3. The shear-induced transverse force on a spherical bubble

3.1. *Experimental determination of the transverse force*

Figure 5 shows a sketch of the force balance on the bubble when it rises near the wall along a slightly inclined path. Assuming a quasi-steady flow evolution, the drag, lift and buoyancy forces must balance. Provided the inclination angle of the path is small, the lift force is almost horizontal, so that the lift and buoyancy forces almost balance the horizontal (z) and vertical (x) components of the drag force, respectively. Neglecting air density, we may then write

$$4\pi\mu R U_s C_{Dx} = \frac{4}{3}\pi R^3 \rho g, \tag{2a}$$

$$4\pi\mu R W C_{Dz} = 2\pi\mu R U_S Re I_L. \tag{2b}$$

In (2a) and (2b) the longitudinal and transverse drag coefficients C_{Dx} and C_{Dz} are defined by normalizing the drag force by its value in the Stokes regime in an unbounded flow, whereas the lift coefficient I_L is defined using an inertial scaling, i.e. writing the lift force as $F_L = 4\pi\rho R^2 I_L U_s^2$. In the case in which the wall lies in the inner region of the flow disturbance, MTL established that the two components of the drag force on a bubble moving close to the wall at zero Reynolds number obey

$$C_{Dx} = 1 + \frac{3}{8}\kappa + \frac{9}{64}\kappa^2 + \frac{27}{512}\kappa^3 + \frac{\gamma}{8}\kappa^2\left(1 + \frac{3}{8}\kappa\right) + O(\kappa^4), \tag{3a}$$

$$C_{Dz} = 1 + \frac{3}{4}\kappa + \frac{9}{16}\kappa^2 + \frac{27}{64}\kappa^3 + O(\kappa^4), \tag{3b}$$

where $\kappa^{-1} = L/R$ is the dimensionless separation and $\gamma = RG/U_s$ is the local relative shear rate. Following TTMM, we assume that for small but non-zero Reynolds numbers and small values of κ, wall-induced and inertial corrections superimpose linearly. Hence we write

$$C_{Dx} = f(Re, \gamma) + \frac{Re}{2} I_{Dx}(\kappa, Re, \gamma) \tag{4a}$$

$$C_{Dz} = f(Re, \gamma) + \frac{Re}{2} I_{Dz}(\kappa, Re, \gamma), \tag{4b}$$

where $f(Re,\gamma)$ is the finite-Re drag coefficient for a clean spherical bubble rising in an unbounded shear flow and I_{Dx} and I_{Dz} are the wall-induced corrections in the vertical and horizontal directions, respectively. Equation (3a,b) indicates that for $Re = 0$, the shear influences the drag only through a wall-induced correction. Moreover, numerical computations performed by Legendre & Magnaudet (1998) in an unbounded shear flow revealed that the shear-induced drag increase is less than 0.5 % for $\gamma = 0.1$ in the whole range $Re \leqslant 5$. As γ is always moderate in our experiments (typically in the range 0.1–0.2), we make use of the above findings to neglect the influence of the shear on $f(Re, \gamma)$. Then we approximate f through the semi-empirical correlation proposed by Mei, Klausner & Lawrence (1994), namely $f(Re) = 1 + \{8Re^{-1} + 0.5(1 + 3.315Re^{-1/2})\}^{-1}$, an expression that smoothly matches the low-Reynolds-number and high-Reynolds-number asymptotic predictions for the drag force. In (4a), the vertical wall-induced correction ReI_{Dx} can be determined on purpose from (2a), since the corresponding right-hand side is known. Nevertheless, given the smallness of γ in the present experiment, the shear-induced correction of $O(\gamma\kappa^2)$ predicted by (3a) cannot exceed a small fraction of the total wall-induced correction to the drag force. Therefore, the corresponding results for I_{Dx} cannot differ significantly from those obtained by TTMM in the case in which the bubble rises near a wall in a liquid at rest. This is why we do not discuss these results here.

In (2b) and (4b), a theoretical input is required to estimate I_{Dz} and finally obtain the lift force. We note that (3b) indicates no influence of the shear on the lateral drag force when the wall lies in the inner region of the disturbance. Assuming that this result still holds when the wall lies in the outer region, we may use the theoretical expression for I_{Dz} obtained by TTMM in the case of a fluid at rest. The corresponding wall correction to the transverse force was obtained in the form of an integral in Fourier space. We found that an accurate fit of this correction, valid for $Re/\kappa < 20$ and agreeing with (3b) in the limit $Re/\kappa \to 0$, is $I_{Dz}(\kappa, Re) = (2\kappa/Re)((3/4) + 1.52 \times 10^{-5}(Re/\kappa)^{3.82}) \exp(-0.312(Re/\kappa))$. With the above approximate expressions for f and I_{Dz} at hand, the experimental determination of R, L, U_s and W and the specification of the shear rate G allow us to evaluate the dimensionless quantities Re, κ and γ from which the lift coefficient I_L may be obtained thanks to (2b). Note that in (2b) the largest experimental uncertainty comes from the transverse velocity W; the corresponding relative error is estimated to range from 2 % to 5 %.

3.2. *Theoretical predictions*

MTL established that when the wall lies in the Stokes region of the flow disturbance, the low-*R*e lift coefficient on a spherical bubble moving parallel to the wall in a linear shear flow is

$$I_L = \frac{1}{16}\left\{\left(1+\frac{\kappa}{8}\right) - \frac{11}{6}\gamma\left(\frac{1}{\kappa}+\frac{9}{8}+\frac{45}{44}\kappa\right) + \frac{11}{18}\gamma^2\left(1+\frac{3}{8}\kappa\right)\right\} + O(\kappa^2). \quad (5)$$

The case in which the wall stands in the outer region of the disturbance was worked out by McLaughlin (1993) who derived the expression of the lift force in the case of a rigid sphere. Since Legendre & Magnaudet (1997) showed that the leading-order inertial lift force on a clean bubble is 4/9 that of a rigid sphere, it is straightforward to extend McLaughlin's result to the case of a bubble. In our notations, the corresponding result reads

$$I_L(l^*, L^*) = -\frac{1}{\pi^2}\frac{G}{|G|}\frac{l^*}{L^*} J\left(\frac{G}{|G|}l^*/L^*, l^*\right), \quad (6)$$

where $L^* = LU_s/\nu$, $l^* = L(|G|/\nu)^{1/2}$ and J is a numerical function given by an integral in Fourier space. The dimensionless lengths L^* and l^* equal $Re/2\kappa$ and $((\gamma Re/2)^{1/2}/\kappa)$, respectively. They represent the convenient outer length scales to be used when the wall lies in the outer region of the disturbance, i.e. in the case $L^* \gg 1$, $l^* \gg 1$, and are associated with slip and shear effects, respectively. Result (6) provides the total lift force on the bubble; i.e. it includes the shear-induced lift force and the wall-induced lateral force the bubble would experience even if rising in a quiescent liquid. Nevertheless both effects do not combine linearly, as the whole process is governed by the Oseen equation that prevents the linear superposition of the flow disturbances associated with two different base flows. McLaughlin (1993) evaluated the function J involved in (6) for various values of the ratio $l^*/L^* = (\nu|G|)^{1/2}/U_s$. Based on his results, we sought an explicit fit of J. The way this fit was obtained is detailed in the Appendix, and (A 2)–(A 5) provide the required expressions to compute I_L, whatever the values of l^* and L^* may be, and compare the corresponding prediction to our measurements.

3.3. *Experimental results*

Figure 6 shows the reduced lift force I_L as a function of L^* for seven bubbles with Reynolds numbers less than 4.0 and two almost opposite shear rates, namely $G \approx \pm 2.3$ s^{-1}. The experimental results agree well with the theoretical prediction for all data sets corresponding to $Re_\infty < 2$, suggesting that this prediction applies at least up to Reynolds number of order unity. Note that figure 6 indicates that the theoretical prediction is still accurate when $L^* < 1$, whereas it was derived under the assumption $L^* \gg 1$. The prediction of Vasseur & Cox (1977) fitted by (A 5) is also showed for comparison. Owing to the mechanical limitations of our device, the shear is fairly weak in these runs and so is l^*/L^*. This is why most of the lateral force is provided by the wall-induced contribution already present in the absence of shear (i.e. (A 4)) rather than by that of the shear (i.e. (A 3)) in the above cases. The data corresponding to $Re_\infty = 2.7$ and 3.5 (which were both obtained with a negative shear) reveal a different trend. Here the lateral force is significantly larger than predicted by the low-*R*e theory. This had to be expected based on the following arguments. First, the DNS results of Legendre & Magnaudet (1998) indicated that beyond $Re \approx 1$ the shear-induced lift force in an unbounded flow does not obey the visco-inertial scaling (6) any more. More precisely, they found that the dependence of I_L with respect to the fluid viscosity quickly becomes much weaker than predicted by (6), in line with

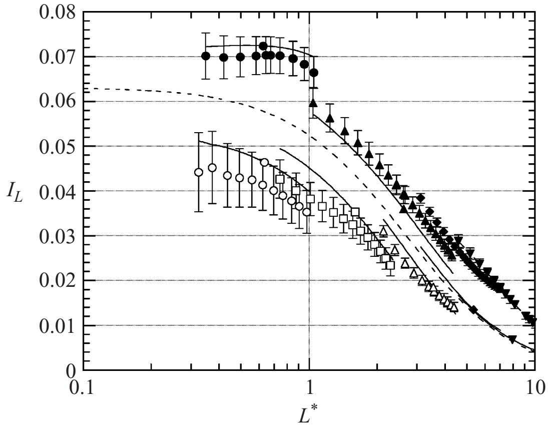

FIGURE 6. The reduced wall-induced lift force I_L versus L^* for $0.5 < Re_\infty < 4.0$ and $L^* < 10$: ●, $Re_\infty = 0.55, l^*/L^* = 0.5$ $(\gamma < 0)$; ○, $Re_\infty = 0.6$, $l^*/L^* = 0.44$ $(\gamma > 0)$; □, $Re_\infty = 1.0, l^*/L^* = 0.3$ $(\gamma > 0)$; ▲, $Re_\infty = 1.5, l^*/L^* = 0.25$ $(\gamma < 0)$; △, $Re_\infty = 1.9$, $l^*/L^* = 0.20$ $(\gamma > 0)$; ◆, $Re_\infty = 2.7, l^*/L^* = 0.16$ $(\gamma < 0)$; ▼, $Re_\infty = 3.5, l^*/L^* = 0.13$ $(\gamma < 0)$. Prediction from (6) using (A 2)–(A 5): —●—, $Re_\infty = 0.55, l^*/L^* = 0.5$; —○—, $Re_\infty = 0.6$, $l^*/L^* = 0.44$; —□—, $Re_\infty = 1.0, l^*/L^* = 0.3$; —▲—, $Re_\infty = 1.5, l^*/L^* = 0.25$; —△—, $Re_\infty = 1.9$, $l^*/L^* = 0.20$; —◆—, $Re_\infty = 2.7, l^*/L^* = 0.16$; —▼—, $Re_\infty = 3.5$, $l^*/L^* = 0.13$. Prediction from (A 5): --------.

the fact that the lift force becomes independent of viscosity for high enough Reynolds number, since the inviscid result of Auton (1987) yields $I_L = -\gamma/3 = -\kappa l^{*2}/3L^*$ in the present notation. Second, Takemura & Magnaudet (2003) examined the repulsive wall-induced force acting on a bubble rising near a vertical wall in a quiescent liquid for $Re > 1$ and found this force to be also larger than that predicted by the low-*Re* theory. This may be explained by the fact that this force evolves essentially as the square of the maximum vorticity at the bubble surface, a quantity which obviously increases with *Re*. Combining both arguments, it is expected that in the case in which $\gamma < 0$, which corresponds to both contributions acting in the same direction, the transverse force should be larger than that predicted by the low-*Re* theory when the Reynolds number increases. This is clearly seen in figure 7 in which the three series of figure 6 corresponding to $Re \geqslant 1.5$ and $\gamma < 0$ are reported. In particular, this figure indicates that the transverse force can be twice as large as that predicted by the low-*Re* theory when the Reynolds number exceeds 2.0.

4. The lift force on a slightly deformed bubble in the low-(L^*, l^*) regime

When a bubble rises near a wall in a quiescent liquid, it deforms into a spheroid with its major axis inclined at nearly 45° from horizontal, owing to the strain created in the gap between the bubble and the wall. When an undisturbed shear is added to the above flow, the deformation of the bubble becomes smaller or larger, depending on the orientation of the shear (see figure 4). Defining the length of the major/minor axis of the spheroid as $(1 \pm \beta)R$, MTL established that under the conditions in which (3) and (5) hold (i.e. $L^* \ll 1$ and $l^* \ll 1$), the magnitude of the leading-mode quasi-steady deformation (i.e. mode 2 in Legendre's expansion) experienced by a bubble

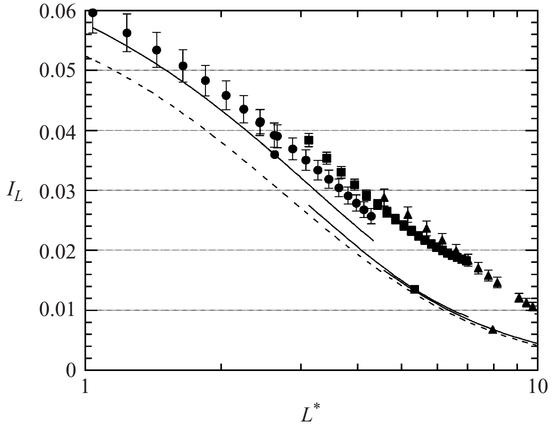

FIGURE 7. The reduced wall-induced lift force I_L versus L^* for $1.0 < Re_\infty < 4.0$ and $L^* < 10$: $Re_\infty = 1.5$, $l^*/L^* = 0.25$ ($\gamma < 0$); ■, $Re_\infty = 2.7, l^*/L^* = 0.16$ ($\gamma < 0$); ▲, $Re_\infty = 3.5, l^*/L^* = 0.13$ ($\gamma < 0$). Prediction from (6) using (A 2)–(A 5): —●—, $Re_\infty = 1.5, l^*/L^* = 0.25$; —■—, $Re_\infty = 2.7, l^*/L^* = 0.16$; —▲—, $Re_\infty = 3.5, l^*/L^* = 0.13$. Prediction from (A 5): --------.

migrating at zero Reynolds number in a wall-bounded linear shear flow is

$$\frac{\beta}{Ca} = \frac{3}{8}\kappa^2 \left\{ 1 + \frac{3}{8}\kappa \left(1 + \frac{3}{8}\kappa + \frac{73}{64}\kappa^2 \right) \right\} + \gamma \left(1 + \frac{3}{8}\kappa^3 \right) + O(\kappa^6, \gamma\kappa^4), \qquad (7)$$

where $Ca = \mu U_s/\sigma$ is the capillary number. The first term on the right-hand side is due to the interaction of the wall with the disturbance flow created by the relative motion between the bubble and the fluid, while the second contribution is the deformation resulting from the imposed shear. Note that we kept terms up to $O(\kappa^5)$ in the first contribution and truncated the second one at $O(\kappa^3)$ because γ is small in our experiments, so that κ^2 is at least as large as γ throughout the near-wall region in which high-order corrections are significant. At large distances from the wall ($\kappa \to 0$), β tends towards $Ca\gamma$, which is the well-known result of Taylor (1932) for a neutrally buoyant drop in an unbounded shear flow. It is worth noting that for small enough negative shears ($\gamma < 0$), (7) predicts that β changes from positive to negative as the separation distance between the bubble and the wall increases. More precisely, since κ is such that $0 < \kappa < 1$, (7) suggests the existence of a particular separation $\kappa_{D0}(\gamma)$ for which β is zero, provided the shear is such that $-2985/5632 \approx -0.53 < \gamma < 0$.

Experimentally, we determined the bubble shape by using pictures recorded in the range $0.02 < Re_\infty < 0.57$ in K100 and K200 silicone oils. The deformation was obtained by expanding the projection of the bubble contour as a function of the polar angle θ, as shown in figure 8 (see TTMM for details). This figure indicates that, in line with the theoretical prediction, the direction of the major axis may change when γ is negative and the separation distance increases. We define the deformation as positive (respectively negative) when the direction of the major axis inclines at 45° (respectively −45°) from horizontal. Therefore, in agreement with (7), the solid line, which corresponds to a positive shear, reveals a positive deformation. In contrast the dotted and dashed–dotted lines, both of which correspond to a negative shear, indicate deformations of opposite signs. This is also in agreement with (7): since κ is less than $\kappa_{D0}(\gamma)$ in the former case, the corresponding deformation is mostly due to

No.	Oil	R (mm)	U_s (mm s^{-1})	κ	Re	Ca	γ	β_{exp}/Ca	β_{th}/Ca	κ_{D0}
1	K100	0.494	6.6	0.38	0.063	0.032	−0.169	−0.076	−0.108	0.60
2	K100	0.494	6.9	0.28	0.066	0.033	−0.163	−0.184	−0.130	0.59
3	K100	0.699	13.2	0.42	0.177	0.063	−0.121	−0.062	−0.044	0.51
4	K100	0.846	15.8	0.80	0.253	0.076	−0.120	0.252	0.246	0.51
5	K100	0.846	16.9	0.68	0.271	0.081	−0.114	0.094	0.122	0.50
6	K100	0.846	17.7	0.57	0.284	0.085	−0.107	0.035	0.046	0.49
7	K100	0.859	14.5	0.83	0.216	0.077	0.128	0.660	0.586	
8	K100	0.859	15.7	0.67	0.234	0.084	0.119	0.424	0.372	
9	K100	0.859	17.0	0.50	0.253	0.090	0.110	0.277	0.236	
10	K100	0.859	17.6	0.42	0.262	0.094	0.106	0.218	0.188	
11	K200	0.647	5.0	0.92	0.036	0.042	−0.273	0.274	0.221	0.70
12	K200	0.520	3.4	0.82	0.019	0.028	0.322	0.980	0.802	
13	K200	0.647	5.4	0.75	0.039	0.046	0.25	0.700	0.609	
14	K200	0.647	5.8	0.61	0.041	0.049	0.23	0.563	0.440	

TABLE 2. Bubble deformation in K100 and K200 silicone oils. The values of the dimensionless parameters take into account the variations of viscosity with room temperature.

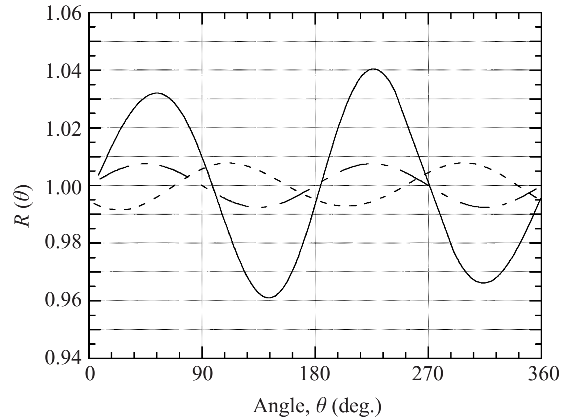

FIGURE 8. The local radius $R(\theta)$ of the two bubbles in figure 4 versus the meridian angle θ ($\theta = 0$ and $\theta = \pi$ are located in the horizontal plane containing the bubble centroid), with $\theta = 0$ (respectively $\theta = \pi$) away from (respectively close to) the wall: — - —, no. 5 in table 2; ——, no. 8 in table 2; --------, no. 2 in table 2.

the shear and is negative, whereas the latter case corresponds to $\kappa > \kappa_{D0}(\gamma)$, so that deformation is mostly due to the presence of the wall and is positive. Also note the difference in the magnitude of the deformation between the solid line ($\beta/Ca \approx 0.42$) and the dashed–dotted line ($\beta/Ca \approx 0.09$), two cases which correspond to almost identical values of Ca, Re, γ and $|\gamma|$. Finally, a closer look at the solid line reveals that points of the surface corresponding to $\theta = 3\pi/4$ and $5\pi/4$ (i.e. close to the wall) experience a larger deformation than the opposite points $\theta = \pi/4$ and $7\pi/4$ located away from the wall. The same is not found in the dashed–dotted line which is close to a pure sinusoid. This difference suggests that close enough to the wall, deformation is affected by nonlinear effects when it exceeds a certain threshold. The experimental parameters of the various runs, together with the experimental (β_{exp}) and theoretical (β_{th}) values of β and the critical separation κ_{D0} are reported in table 2. This table shows that the magnitude of the experimental deformation agrees fairly well with

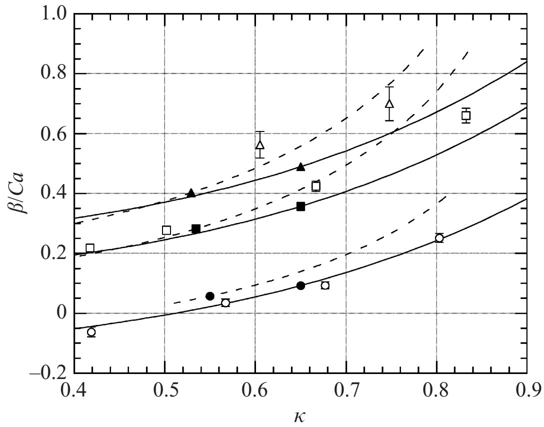

FIGURE 9. The normalized deformation β/Ca as a function of κ for two bubbles corresponding to conditions $Re_\infty = 0.44, \gamma \approx \pm 0.120$ and $Re_\infty = 0.04, \gamma \approx 0.240$, respectively. Experimental values are for: □, $\gamma \approx 0.120$ (nos. 7–10 in table 2), ○, $\gamma \approx -0.120$ (nos. 3–6 in table 2); △, $\gamma \approx 0.240$ (nos. 13 and 14 in table 2). Theoretical values are for: —■—, $\gamma = 0.120$; —●—, $\gamma = -0.120$; —▲—, $\gamma = 0.240$. Numerical values are for: - - -■- - -, $\gamma \approx 0.120$; - - - ●- - -, $\gamma \approx -0.120$; - - -▲- - -, $\gamma \approx 0.240$.

the theoretical prediction, even though the difference may reach 40 % in some cases, owing to experimental uncertainties discussed in § 2. Cases 1–6 and case 11 in which the outer shear is negative extend the conclusions of figure 8 concerning the possibility for the deformation to change sign as the separation distance increases. Indeed, in cases 1–3 for which κ is smaller than $\kappa_{D0}(\gamma)$ the deformation is found to be dominated by the effect of the undisturbed shear, whereas in cases 4, 5, 6 and 11, where κ is larger than $\kappa_{D0}(\gamma)$, β has opposite signs, owing to the dominant effect of the wall. Not unexpectedly, the deformation is very small in cases 3 and 6 in which κ is close to $\kappa_{D0}(\gamma)$. Figure 9 shows how the deformation evolves with κ in cases 3–10 (selected because they correspond to quite similar values of $|\gamma| \approx 0.12$) and in cases 13 and 14 corresponding to a higher shear rate $|\gamma| \approx 0.24$. As predicted by (7), the deformation is found to be larger and positive, whatever the value of κ may be, when the shear rate is positive, while it changes sign for a certain separation when $\gamma < 0$. Note that (7) is found to predict well the deformation up to $\kappa \approx 0.8$, i.e. for separations corresponding to a gap as small as about $0.25R$.

The deformation of bubbles migrating in a wall-bounded linear shear can also be evaluated numerically. Wang & Dimitrakopoulos (2006) developed a three-dimensional interfacial spectral boundary element algorithm and studied the motion and deformation of drops of arbitrary viscosity in such flows under Stokes flow conditions. Dimitrakopoulos (2007) then improved this technique by making its time integration fully implicit, which allows the use of much larger time steps. We employed the latter method to compute the deformation of bubbles in our experimental configuration. The spectral boundary element configuration was similar to that presented in Wang & Dimitrakopoulos (2006). The accuracy of the computational results was verified by employing various time and space discretizations. These tests showed that the results are accurate to at least three significant digits, and thus if we include them on the same plot, they show no difference. Note that the limitation of these computations to creeping flow conditions is not a severe restriction in our case because MTL showed that provided Re and Ca are both small and the wall lies in the inner region of the disturbance, the leading-order deformation experienced by the bubble results from the creeping flow solution of the problem. This makes the boundary element approach appropriate to obtain an independent determination of the deformation under present flow conditions.

The deformation β can be estimated from the numerical results by calculating the ratio $(\zeta - 1)/(\zeta + 1)$, where ζ denotes the ratio between the bubble's longest and shortest semi-axes, i.e. the maximum and minimum distance from the bubble centroid to the interface. Note that, in general, these longest and shortest semi-axes lie near, but not exactly at, $\theta = \pm \pi/4$. Strictly speaking, this estimate of the deformation slightly differs from that obtained using the coefficients of the mode 2 in the Fourier expansion of the bubble contour because it includes higher-order effects. As shown in figure 9, the calculated deformations are in good agreement with the experimental determination for positive shears, except very close to the wall, whereas they slightly overestimate the deformation for negative shears. These differences are most likely due to the higher-order effects mentioned above.

As is well known, deformation may also induce a lift force, even at zero Reynolds number, because it breaks the fore–aft symmetry of the flow. MTL established that when the wall lies in the Stokes region of the flow disturbance (i.e. $L^* \ll 1$ and $l^* \ll 1$), the total lift force acting on a slightly deformed bubble moving parallel to a wall is

$$I_L = I_L^{Sp} + \frac{1}{20}\frac{Ca}{Re}\left\{3\kappa^2\left(1+\frac{3}{2}\kappa\right) + 8\gamma\left(1+\frac{3}{8}\kappa+\frac{9}{64}\kappa^2\right) + \frac{169}{7}\gamma^2\kappa^2\right\} + O(\kappa^4, \gamma\kappa^3), \tag{8}$$

where I_L^{Sp} is the lift force acting on a spherical bubble standing at the same position in the same flow, as given by (5). (Actually there is a misprint in the original equation concerning the prefactors of the κ and κ^2 terms within the second parenthesis; the correct prefactors are those of (8)). The term proportional to Ca in (8) is entirely due to mode 2 deformation, as MTL showed that higher-order modes only start to contribute to the lift force only at $O(\kappa^4)$. The first term within parentheses in (8) results from the slip between the bubble and the surrounding flow, while the other two are due to the shear. Note that the first and last terms are entirely caused by the interaction with the wall, while the effect that remains at large separation is a lift force with the same sign as the shear. This aspect contrasts with the inertial contribution of the shear to the total lift force. Indeed, as (5) indicates, a positive shear induces a negative (i.e. attractive) inertial lift contribution when the slip velocity is positive (as in our experiment), while it results in a positive (i.e. repulsive) deformation-induced lift force. Therefore, for small enough Ca/Re, there is a critical separation κ_c at which the two shear-induced contributions cancel each other. In such a situation, (8) predicts that the total lift force is directed away from the wall for $\kappa > \kappa_c$ and towards it for larger separations, since the inertial shear-induced contribution then becomes dominant owing to the κ^{-1} term in (5).

Figure 10 shows how the total lift force evolves with separation for three different bubbles experiencing either a positive or a negative shear rate. Note that by letting the belts rest, we checked that the distribution of the transverse force in the absence of shear, say I_{L0}, agrees well with that obtained in a quiescent fluid by TTMM. The results reported in figure 10 clearly show that for a given magnitude $|\gamma|$ of the shear, the lateral force is larger when the shear is positive. This force also strongly increases as the wall is approached. For positive shear rates, the total transverse force is dominated by the deformation-induced contribution over the whole range

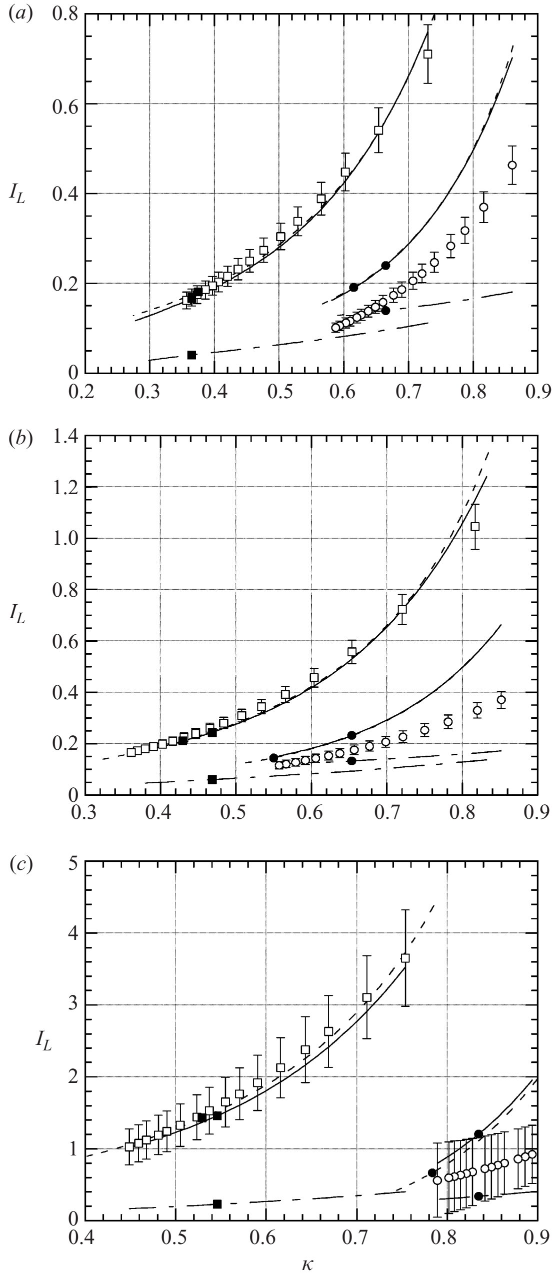

FIGURE 10. (*a*) The wall-induced lift force I_L versus κ in the regime $l^* \ll 1$, $L^* \ll 1$. (*a*) $R = 0.67$ mm, $\gamma = \pm 0.14$, K100 oil. Experimental values are for: □, $\gamma = 0.140$; ○, $\gamma = -0.140$. Theoretical predictions (8) are for: —■—, $\gamma = 0.140$; —●— $\gamma = -0.140$. Computational predictions are for: —■— $\gamma = 0.140$; —●— $\gamma = -0.140$. Prediction from correlation (11) are for: ---■--- $\gamma = 0.140$; ---●--- $\gamma = -0.140$. (*b*) Same as for $R = 0.85$ mm, $\gamma = \pm 0.11$ in K100 oil. (*c*) Same as for $R = 0.65$ mm, $\gamma = \pm 0.24$ in K200 oil.

of separations, since it is positive everywhere in spite of the negative contribution provided by the inertial contribution.

The theoretical prediction (8) is also plotted in figure 10 for comparison. The discrepancy with experimental data is obvious, except for negative shear rates, where (8) is found to predict the order of magnitude of the transverse force reasonably well for $\kappa < 0.65$, approximately. The increase of I_L when the bubble comes closer to the wall is clearly underpredicted. This may be interpreted as a simple limitation of the truncation of (8) at $O(\kappa^4, \gamma\kappa^3)$, while higher-order contributions may become important or even dominant when $\kappa \rightarrow 1$. However the severest discrepancy between (8) and the experimental data is found to concern the sign of the variations of I_L with γ, since (8) suggests a decrease of I_L when γ increases, at odds with the experimental trend. For the range of shear rates covered by present experiments, the evolution of I_L with γ as predicted by (8) reveals a dominant role of inertia because it corresponds to a negative value of the derivative $\mathrm{d}I_L/\mathrm{d}\gamma$, just as indicated by (5). In contrast, experimental data unambiguously reveal that $\mathrm{d}I_L/\mathrm{d}\gamma$ is positive, i.e. that deformation effects are dominating the transverse force. Equation (8) was obtained independently through two different analytical techniques. It was carefully checked and was found to reduce to known results in the case of a neutrally buoyant bubble.

To clarify the situation we used the spectral boundary element code mentioned above, which provides a third, independent, determination of the lateral force. Since the corresponding computations were performed at zero Reynolds number, they only provide the deformation-induced migration velocity, say W_{num}. Therefore, to obtain the total lift force at the current experimental Reynolds number, we use (2*b*) and estimate I_L as

$$I_L = I_L^{Sp} + 2W_{num}Re^{-1}C_{Dz}/U_S. \tag{9}$$

As shown by MTL, this linear superposition is rigorously justified when both the capillary and Reynolds numbers are small and have a similar order of magnitude. The corresponding predictions for I_L are plotted in figure 10. The numerical predictions provide the correct order of magnitude and variation of the lateral force with both γ and κ. In particular, these predictions are found to agree well with the experimental data over the whole range of κ for positive shear rates. The difference increases for negative γ, where the numerical values of I_L are larger than the experimental data by 20–40 %, especially when the separation becomes small. This is most likely due to the smaller magnitude of the force in this case, which makes the consequences of experimental errors and approximations, such as that involved in the linearization (9), more sensitive.

The general agreement between experimental and computational results leads us to the conclusion that the theoretical prediction (8) is in error, even though the origin of this error is still unknown (see § 5 for a discussion on this point). This view is reinforced by the fact that what is left from (8) in the shearless case does not agree with the experimental lateral force measured by TTMM in a quiescent liquid or with the corresponding numerical predictions of Wang & Dimitrakopoulos (2006). Given the failure of (8) we found it useful, at least provisionally, to correlate empirically the numerical predictions for the transverse force. To this end, we successively correlated the values I_{LD0} of the deformation-induced lift force in a quiescent liquid and those of the contribution I_{LDS} due to the shear. Assuming that all effects are additive, as in (8), the total lift force in the regime of low Reynolds and capillary numbers may then be written in the form $I_L = I_L^{Sp} + I_{LD0} + I_{LDS}$. Assuming in addition that the leading-order scaling predicted by (8) is correct, $I_{LD0}Re/(2\kappa^2 Ca)$ is expected to depend only on κ.

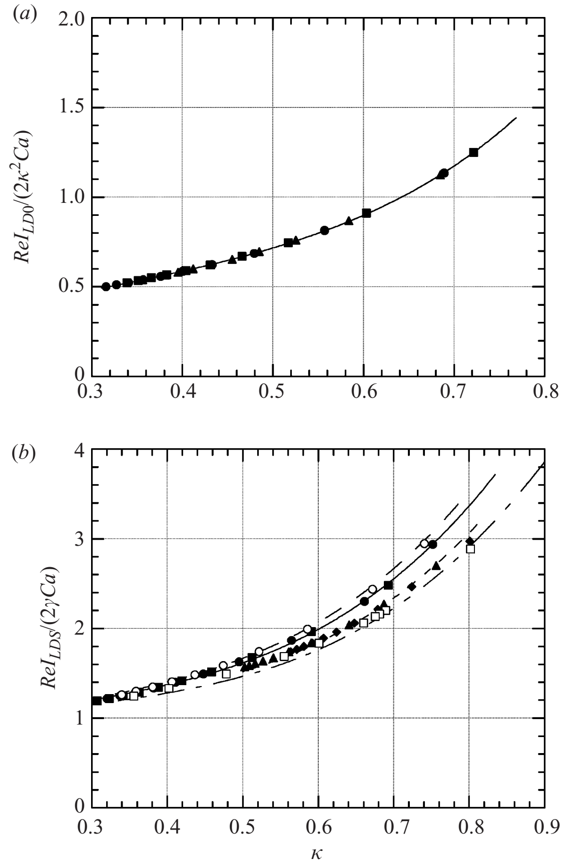

FIGURE 11. Numerical predictions for I_{LD0} and I_{LDS} versus separation κ for various shear rates and bubble radii (in K100 oil when unspecified). (*a*) $ReI_{LD0}/(2\kappa^2 Ca)$ for: ●, $R = 0.83$ mm; ■, $R = 0.65$ mm; ▲, $R = 0.65$ mm in K200; predictions from (10*a*) are symbolized by ——. (*b*) $ReI_{LDS}/(2\gamma Ca)$ for: ●, $R = 0.86$ mm and $G = 2.3\ \mathrm{s}^{-1}$; ■, $R = 0.64$ mm and $G = 1.9\ \mathrm{s}^{-1}$; ▲, $R = 0.85$ mm and $G = -2.15\ \mathrm{s}^{-1}$; ◆, $R = 0.71$ mm and $G = -2.1\ \mathrm{s}^{-1}$; ○, $R = 0.65$ mm and $G = 2.1\ \mathrm{s}^{-1}$ in K200; □, $R = 0.65$ mm and $G = -2.1\ \mathrm{s}^{-1}$ in K200. Prediction from $G(\kappa) + \gamma H(\kappa)$ are for: ——, $\gamma = 0.140$; -----, $\gamma = -0.140$; - - - - -, $\gamma = 0.240$; — - —, $\gamma = -0.240$.

Hence we plot the numerical values of $I_{LD0}Re/(2\kappa^2 Ca)$ for three typical experimental conditions obtained by varying the bubble radius and liquid viscosity. As shown in figure 11(*a*), the three series of values almost collapse, so that $I_{LD0}Re/(2\kappa^2 Ca)$ may be correlated in the form $F(\kappa)$ as

$$F(\kappa) = 0.25 + 0.39\kappa + 2.43\kappa^2 - 5.43\kappa^3 + 5.52\kappa^4. \qquad (10a)$$

Similarly, assuming that the leading-order scaling of I_{LDS} in (8) is correct, we plot the values of $I_{LDS}Re/2\gamma Ca$ for six different experimental conditions corresponding to different values of the bubble radius, shear rate and liquid viscosity. As shown in figure 11(*b*), the various series of data almost collapse, except for $\kappa > 0.6$ where an influence of the sign of the shear is detected. This had to be expected, given the presence of a term proportional to $\gamma^2\kappa^2$ in (8). Making use of the sum and the difference of these series of data, we correlate them in the form $G(\kappa) + \gamma H(\kappa)$ with

$$G(\kappa) = 0.53 + 3.79\kappa - 8.25\kappa^2 + 9.63\kappa^3, \quad H(\kappa) = 1.8\kappa^2. \qquad (10b)$$

Using these results and considering that the inertial contribution to the transverse force is correctly predicted by (5), we finally obtain the total lift force I_L as

$$I_L = I_L^{Sp} + 2\frac{Ca}{Re}(\kappa^2 F(\kappa) + \gamma G(\kappa) + \gamma^2 H(\kappa)). \tag{11}$$

Values of the reduced transverse force predicted by (11) for the experimental conditions considered in figure 10 are also reported in figure 11. The whole set of experimental data is found to be reasonably well approximated by (11). As already noticed during the direct comparison with the computational results, the agreement is especially good for positive shears, while experimental values of the force are somewhat smaller than predicted by (11) for negative shears, probably because they result in significantly smaller values of the force and hence in larger relative experimental errors.

5. Summary and conclusions

We investigated experimentally the migration and deformation of bubbles rising in a wall-bounded linear shear flow at low-but-finite Reynolds number. We produced a quasi-linear shear flow by moving two parallel belts in opposite directions and accurately measured the bubble radius, contour, rising speed and separation distance from the wall using a high-precision optical device travelling with the bubble. Thereby the quasi-steady transverse or lift component of the hydrodynamic force was determined in the range $0.1 < Re < 4$. In the parameter range in which the bubbles keep a spherical shape, we compared our experimental results with an approximate fit directly based on an extension of the theory of McLaughlin (1993), originally derived for a solid sphere moving in a wall-bounded shear flow. The comparison indicates that the measured lift force agrees well with the theoretical prediction up to $Re \approx 1.5$. Beyond this Reynolds number, the lift force becomes larger than that predicted by the low-Re theory when the shear is negative. This is in line with the known behaviour of both the shear-induced lift force in an unbounded flow and the wall-induced transverse force in a fluid at rest at infinity.

We finally studied the quasi-steady deformation and deformation-induced migration of bubbles moving in high-viscosity liquids in the regime in which the wall stands in the Stokes region of the flow disturbance. In parallel, we computed the quasi-steady evolution of deformable bubbles moving in a wall-bounded linear shear flow at zero Reynolds number, using the spectral boundary element method developed by Dimitrakopoulos (2007). The experimental deformation, which, depending on the sign of the shear, may be larger or smaller than that of a bubble moving in a quiescent liquid, was found to agree quantitatively well both with the theoretical prediction of MTL and with the computational predictions. In contrast, the deformation-induced lift force which is increased (respectively decreased) by a positive (respectively negative) shear, turned out to be significantly larger than that predicted by the available theory and agrees quantitatively well with the computational prediction. What we learnt regarding the failure of the theoretical prediction (8) may be summarized as follows: (*a*) The discrepancy does not result from a finite-Re correction affecting the deformation-induced transverse force, since the computations were performed under creeping flow conditions, and their results agree well with those of the low-but-finite-Re experiments. Also we directly compared the prediction of (8) for $Re = 0$ (which is equation (38) of MTL) with the computational results and found that the discrepancy persists. (*b*) The discrepancy does not seem to be due to a limitation of the theory with respect to the value of the capillary number. Computations not reported in the paper were performed for values of Ca 10 times too small than those involved in the experiments. The comparison with theoretical predictions displayed the same consistent discrepancy as that found in figure 10. Nevertheless we are still exploring this possibility by running computations with even smaller values of Ca. (*c*) Finally, keeping in mind that the various series of data reported in figure 11 were normalized using the scaling predicted by (8), the successful collapse observed in the figure indicates that the leading-order scaling of all contributions to the deformation-induced transverse force is correctly predicted by the theory. Therefore the problem in the theory clearly lies in the numerical prefactors (which are typically 2.5–3 times too small and have to be provisionally replaced by those given in (10) and (11)), not in the scaling.

Combined with available theories and/or computations, present results allow us to understand how slip and shear contribute to the quasi-steady inertial and deformation-induced migration of bubbles rising parallel to a wall in a linear shear flow at low-to-moderate Reynolds number. These results, together with the theoretical expressions and semi-empirical correlations they helped to build and/or validate, may now be used to obtain closure laws for predicting the motion of small bubbles rising in more complex wall-bounded flows which may locally be regarded as linear.

P. Dimitrakopoulos was supported in part by the US National Science Foundation. The donors of the American Chemical Society's Petroleum Research Fund are acknowledged for partial support of this research. Some computations were performed on multiprocessor supercomputers provided by the National Center for Supercomputing Applications in Illinois.

Appendix. Explicit fit of the function J in (6)

Since the function J in (6) is given by an integral in Fourier space, it is convenient for practical purpose to fit it explicitly. We sought the fit of J based on the following remarks. First, it is physically relevant to split J in the form $J_0 + J_S$, where the contribution J_S changes sign when either G or U_s reverses, whereas the contribution J_0 keeps a constant sign. Basically J_0 results from the wall-induced force of Vasseur & Cox (1977) altered by the shear, whereas J_S results from the Saffman lift force altered by the wall. A physical interpretation of these two contributions in terms of the fluid displaced laterally in the bubble wake and the resulting transverse pressure gradient may be found on pp. 140 and 143 of MTL, respectively. For large l^*, J_S must converge towards the function J_U involved in the expression of the shear-induced lift force on a sphere translating in an unbounded linear shear flow (McLaughlin 1991), whereas J_0 has to tend to zero. Comparing (6) with (5) evaluated in the outer limit $\kappa \to 0$ indicates that for $l^* \to 0$ one must have

$$J_S \to \frac{11}{96}\pi^2 l^*, \quad J_0 \to -\frac{\pi^2}{16}\frac{G}{|G|\,\varepsilon}, \tag{A 1}$$

where $\varepsilon = l^*/L^* = (\nu\,|G|)^{1/2}/U_s$. McLaughlin (1991) computed $J_U(\varepsilon)$ based on the Oseen approximation and provided asymptotic approximations valid at both large and small ε. Legendre & Magnaudet (1998) evaluated numerically the lift force on a spherical bubble in an unbounded linear shear flow from the full Navier–Stokes equations. Figure 12 shows the variations of $J_U(\varepsilon)$ as a function of ε obtained by both groups. The theoretical and numerical evolutions are in good agreement for

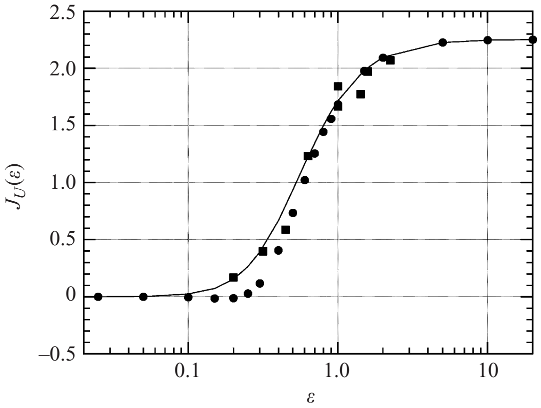

FIGURE 12. The plot of $J_U(\varepsilon)$ versus $\varepsilon = l^*/L^*$: ●, the theoretical solution of McLaughlin (1991); ■, numerical data from Legendre & Magnaudet (1998); ——, prediction from (A 2).

$\varepsilon > 0.5$. In contrast they significantly differ for low ε, where the theoretical solution suggests that the shear-induced lift force changes sign, a trend which is not displayed by the DNS results. The reason for this disagreement is probably that the Oseen approximation is not sufficiently accurate to evaluate properly the tiny lift force that subsists at such low shear rates. In particular, this approximation cannot capture the so-called second-order Saffman lift force of $O(R^3 G U_s \nu^2)$ which results from the flow disturbance in the inner region in which the distance r to the bubble centre is such that $r < \mathrm{Min}\{(\nu/|G|)^{1/2}, \nu/U_s\}$ (Saffman 1965, 1968). Based on their numerical results at various ε for $Re < 1$ and on the results of McLaughlin (1991) for $\varepsilon > 0.8$, Legendre & Magnaudet (1998) fitted $J_U(\varepsilon)$ in the form

$$J_U(\varepsilon) = J_U(\infty)(1 + 0.2\varepsilon^{-2})^{\frac{-3}{2}} = 2.255(1 + 0.2\varepsilon^{-2})^{-1.5}. \tag{A 2}$$

This fit is also displayed in figure 12.

In the wall-bounded case, the shear-induced lift force is gradually altered by the wall as l^* decreases, until it falls linearly to zero for small enough l^* as indicated by the first part of (A 1). Based on the results tabulated by McLaughlin (1993), we empirically express this variation in the form

$$J_S(l^*, \varepsilon) = \left\{1 - \exp\left(-\frac{11\pi^2}{96}\frac{l^*}{J_U(\varepsilon)}\right)\right\} J_U(\varepsilon). \tag{A 3}$$

The second contribution to J, J_0, keeps a constant sign, whatever the respective signs of the shear and slip velocity may be. This contribution is entirely due to the wall and must tend towards the lift force in an unsheared flow, whatever the value of l^*/ε may be, when the shear is negligibly small, i.e. in the limit $\varepsilon \to 0$. It must also satisfy the second part of (A 1), whatever the value of ε may be, in the limit $l^* \to 0$. Therefore, based again on the numerical results provided by McLaughlin (1993), we found that J_0 may be fitted in the form

$$J_0(l^*, \varepsilon) = -\pi^2 \frac{G}{|G|\,\varepsilon} \exp(-0.22\varepsilon^{0.8} l^{*2.5}) I_{L0}(l^*/\varepsilon), \tag{A 4}$$

where I_{L0} denotes the transverse force coefficient in the unsheared case. The rapid decrease of εJ_0 as ε increases indicates that the shear tends to damp the corresponding wall-induced contribution to the lateral force. TTMM expressed I_{L0} in the form of

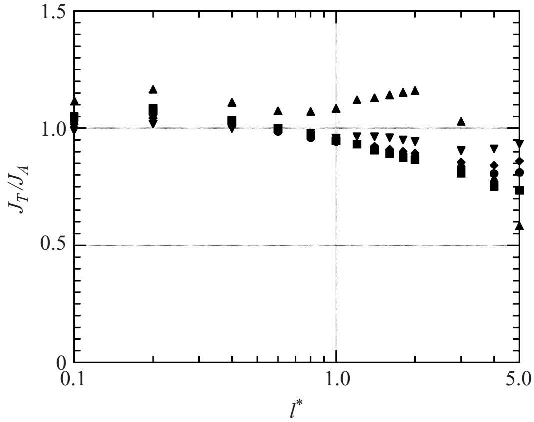

FIGURE 13. The plot of J_T/J_A as a function of l^* for various $\varepsilon = l^*/L^*$: ▲, $\varepsilon = 0.2$; ■, $\varepsilon = 0.6$; ●, $\varepsilon = 0.8$; ◆, $\varepsilon = 1.0$; ▼, $\varepsilon = 2.0$.

an integral in Fourier space. This integral may also be fitted to obtain an explicit expression. For $L^* = l^*/\varepsilon < 10$, an accurate fit for I_{L0} was found to be

$$I_{L0}\left(L^*\right) = \left(\frac{1}{16} + 3.21 \times 10^{-7} L^{*4.58}\right) \exp(-0.292L^*). \tag{A 5}$$

This completes the fitting of the inertial lift force over the range of l^* and L^* (or ε) of interest in our experiments. Using (A 2)–(A 5), an approximate value of J, say J_A, may be obtained, whatever the separation distance, slip velocity and shear rate may be, in the form $J_A = J_0 + J_S$. Figure 13 shows how J_A compares with the theoretical values of J computed by McLaughlin (1993), say J_T. The difference is within 15 % for all ε when l^* is smaller than 1 and becomes larger than 20 % only for the smallest two values of ε when $l^* > 3$, a range of parameters which is not reached in the low-*Re* data discussed above. Therefore we consider that the above fits provide reasonable approximations of J and use them to evaluate I_L through (6).

REFERENCES

AUTON, T. R. 1987 The lift force on a spherical body in rotational flow. *J. Fluid Mech.* **183**, 199–218.

BENEDICT, R. P., ABERNETHY, R. B. & OSOLSOBE, G. 1985 Measurement uncertainty. *Performance Test Code Rep.* 19-1. ANSI/ASME.

CHERUKAT, P. & MCLAUGHLIN, J. B. 1994 The inertial lift on a rigid sphere in a linear shear flow field near a flat wall. *J. Fluid Mech.* **263**, 1–18.

COX, R. G. & BRENNER H. 1968 The lateral migration of solid particles in Poiseuille flow. Part 1. *Theory Chem. Engng Sci.* **23**, 147–173.

COX, R. G. & HSU S. K. 1977 The lateral migration of solid particles in a laminar flow near a plate. *Intl J. Multiphase Flow* **3**, 201–222.

DIMITRAKOPOULOS, P. 2007 Interfacial dynamics in Stokes flow via a three-dimensional fully-implicit interfacial spectral boundary element algorithm. *J. Comput. Phys.* **225**, 408–426.

HOGG, A. J. 1994 The inertial migration of non-neutrally buoyant spherical particles in two-dimensional shear flows. *J. Fluid Mech.* **272**, 285–318.

LEAL, L. G. 1980 Particle motions in a viscous fluid. *Annu. Rev. Fluid Mech.* **12**, 435–476.

LEGENDRE, D. & MAGNAUDET, J. 1997 A note on the lift force on a spherical bubble or drop in a low-Reynolds-number shear flow. *Phys. Fluids* **9**, 3572–3574.

LEGENDRE, D. & MAGNAUDET, J. 1998 The lift force on a spherical bubble in a viscous linear shear flow. *J. Fluid Mech.* **368**, 81–126.

MAGNAUDET, J., TAKAGI, S. & LEGENDRE, D. 2003 Drag, deformation and lateral migration of a buoyant drop moving near a wall. *J. Fluid Mech.* **476**, 115–157.

MCLAUGHLIN, J. B. 1991 Inertial migration of a small sphere in linear shear flows. *J. Fluid Mech.* **224**, 261–274.

MCLAUGHLIN, J. B. 1993 The lift on a small sphere in wall-bounded linear shear flows. *J. Fluid Mech.* **246**, 249–265.

MEI, R., KLAUSNER, J. F. & LAWRENCE, C. J. 1994 A note on the history force on a spherical bubble at finite Reynolds number. *Phys. Fluids* **6**, 418–420.

SAFFMAN, P. G. 1965 The lift on a small sphere in a slow shear flow. *J. Fluid Mech.* **22**, 385–400.

SAFFMAN, P. G. 1968 The lift on a small sphere in a slow shear flow: corrigendum. *J. Fluid Mech.* **31**, 624.

SEGRE, G. & SILBERBERG, A. 1962*a* Behaviour of macroscopic rigid spheres in Poiseuille flow. Part 1. Determination of local concentration by statistical analysis of particle passages through crossed light beams. *J. Fluid Mech.* **14**, 115–135.

SEGRE, G. & SILBERBERG, A. 1962*b* Behaviour of macroscopic rigid spheres in Poiseuille flow. Part 2. Experimental results and interpretation. *J. Fluid Mech.* **14**, 136–157.

SERIZAWA, A., KATAOKA, I. & MICHIYOSHI, I. 1975 Turbulence structure of air-water bubbly flow. Part 2. Local properties. *Intl J. Multiphase Flow* **2**, 235–246.

TAKEMURA, F. & MAGNAUDET, J. 2003 The transverse force on clean and contaminated bubbles rising near a vertical wall at moderate Reynolds number. *J. Fluid Mech.* **495**, 235–253.

TAKEMURA, F., TAKAGI, S., MAGNAUDET, J. & MATSUMOTO, Y. 2002 Drag and lift forces on a bubble rising near a vertical wall in a viscous liquid. *J. Fluid Mech.* **461**, 277–300.

TAKEMURA, F. & YABE, A. 1998 Gas dissolution process of spherical rising gas bubbles. *Chem. Engng Sci.* **53**, 2691–2699.

TAKEMURA, F. & YABE, A. 1999 Rising speed and dissolution rate of a carbon dioxide bubble in slightly contaminated water. *J. Fluid Mech.* **378**, 319–334.

VASSEUR, P. & COX, R. G. 1977 The lateral migration of spherical particles sedimenting in a stagnant bounded fluid. *J. Fluid Mech.* **80**, 561–591

WANG, Y. & DIMITRAKOPOULOS, P. 2006 A three-dimensional spectral boundary element algorithm for interfacial dynamics in Stokes flow. *Phys. Fluids* **18**, 082106.